Computerized Medical Imaging and Graphics 38 (2014) 202–210

Computerized Medical Imaging and Graphics

journal homepage: www.elsevier.com/locate/compmedimag

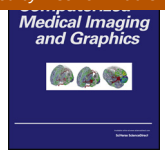

Normalized gradient fields for nonlinear motion correction of DCE-MRI time series

Erlend Hodneland[a,*], Arvid Lundervold[a,b], Jarle Rørvik[b,c], Antonella Z. Munthe-Kaas[d]

[a] Department of Biomedicine, University of Bergen, Bergen, Norway
[b] Department of Radiology, Haukeland University Hospital, Bergen, Norway
[c] Department of Clinical Medicine, University of Bergen, Bergen, Norway
[d] Department of Mathematics, University of Bergen, Bergen, Norway

ARTICLE INFO

Article history:
Received 28 May 2013
Received in revised form 5 October 2013
Accepted 2 December 2013

Keywords:
DCE-MRI
Image registration
MR renography
Normalized gradients
Mutual information

ABSTRACT

Dynamic MR image recordings (DCE-MRI) of moving organs using bolus injections create two different types of dynamics in the images: (i) spatial motion artifacts due to patient movements, breathing and physiological pulsations that we want to counteract and (ii) signal intensity changes during contrast agent wash-in and wash-out that we want to preserve. Proper image registration is needed to counteract the motion artifacts and for a reliable assessment of physiological parameters. In this work we present a partial differential equation-based method for deformable multimodal image registration using normalized gradients and the Fourier transform to solve the Euler–Lagrange equations in a multilevel hierarchy. This approach is particularly well suited to handle the motion challenges in DCE-MRI time series, being validated on ten DCE-MRI datasets from the moving kidney. We found that both normalized gradients and mutual information work as high-performing cost functionals for motion correction of this type of data. Furthermore, we demonstrated that normalized gradients have improved performance compared to mutual information as assessed by several performance measures. We conclude that normalized gradients can be a viable alternative to mutual information regarding registration accuracy, and with promising clinical applications to DCE-MRI recordings from moving organs.

1. Introduction

Image registration is the task of aligning an input image to a reference image by applying a proper spatial transformation to the input image, maximizing a similarity measure between the two images [1]. It is a crucial processing step in many real world applications, especially in medicine for the alignment of images from the brain [2–4], kidneys [5–7], colon [8], prostate [9,10], lungs [11,12] and the heart [13,14]. After alignment, image-derived measurements inside anatomically fixed regions of interest can be compared for further analysis. The focus of this work is on DCE-MRI, an *in vivo* measurement technique enabling voxel-wise assessment of physiological parameters like plasma flow and plasma volume, as well as permeability, extra-vascular volume, permeability-surface area product, and the glomerular filtration rate (GFR) in the kidney. The GFR is a measure of filtrated fluid in the renal glomeruli, and is an important diagnostic and prognostic indicator of kidney function. Therefore, as a model system for co-registration of renal DCE-MRI time series, we study the effects of various cost functions on the accuracy of estimated GFR. Without a proper motion correction of the potentially severe and nonlinear displacement of the kidney, assessment of voxelwise, functional kidney parameters becomes invalid [15]. In a more general context, correction of motion corrupted DCE-MRI time series is important for tracer-based pharmacokinetic modeling and reliable estimation of physiological parameters (such as the GFR). Moreover, the motion correction is particularly challenging in DCE-MRI due to the combination of temporal and spatial signal change upon bolus passage. Proper co-registration is therefore still an open problem in many instances [16].

Preferably, motion correction of DCE-MRI kidney time series should be performed by automated and non-linear registration methods. Non-linearity in the registration is important since the breathing, peristaltic movements and cardiovascular pulsations are non-linear displacements. Automation is desired since 4D time series are very large data sets. Substantial manual intervention of such large data sets is excessively time consuming and also subject to operator dependent variations.

* Corresponding author. Tel.: +47 55586732.
E-mail address: erlend.hodneland@uib.no (E. Hodneland).

0895-6111
http://dx.doi.org/10.1016/j.compmedimag.2013.12.007

Previous reports show that motion correction of DCE-MRI time series has been performed using various approaches. Spatial alignment of the time series has been obtained by effortful intervention using manual segmentations [17], by modeling the motion as head-to-feet only [18], using normalized cross-correlation and isocontours from segmentation [19], or by using mutual information (MI) [20–22] or normalized mutual information (NMI) [23]. Song et al. [24] developed a multi-step 3D registration model consisting of anisotropic diffusion, wavelet edge detection and Fourier based registration. There are also studies applying gradient information as the cost functional [25,26], or combinations of NMI and the gradient magnitude [27].

Another gradient depending cost function is *normalized gradient fields* (NGF), proposed by Haber and Modersitzki [26,28]. Normalized gradient fields incorporate co-aligned gradient vectors of the input and target image and are therefore essentially intensity independent. Due to this property, NGF is suitable for multimodal image registration and it is potentially very promising as a cost functional for registration of DCE-MRI time series. The use of NGF for *rigid* motion correction of DCE-MRI, was explored by Zikic et al. [15]. Since a translational representation preserves the shape of the kidney, they concluded that motion correction based on template-matching, solving for translational parameters only, was superior to deformable methods with a larger number of degrees of freedom. However, due to various degree of nonlinear and deformable movements of kidney, we consider the development of deformable registration algorithms to be of high importance for DCE-MRI. We have therefore developed and tested a *deformable* NGF model for motion correction of DCE-MRI time series.

As far as similarity measures are concerned, MI has been extensively used for co-registration of DCE-MRI images. However, the use of mutual information can in principle be problematic since MI is a global similarity measure relying on a consistent intensity mapping of the whole image [29]. To clarify the goodness of MI, we therefore provide a comprehensive registration evaluation scheme, comparing the similarity measures NGF and MI [30–32] within the same deformable fluid registration framework. We chose MI for comparison since it is considered to be a versatile method of choice for multimodal image registration. It has also been extensively used for co-registration of DCE-MRI in the past [20–23]. However, the performance of MI as cost function for co-registration of DCE-MRI time series has, to our knowledge, not been properly evaluated. Therefore, in this work, we perform a rigorous comparison of MI with NGF. The performance of MI and NMI seems to be comparable [33] and we have therefore explored MI only.

Assessment of registration performance in DCE-MRI motion correction has been poorly addressed, mainly using checkerboard images for visual assessment or pharmaco-kinetic modeling in some reports [21,34–37]. A major impediment is the lack of standardized "ground truth" images for multimodal registration. It was claimed in [38] that landmarks and labelled anatomical structures are best suited for registration evaluation if they can be rigorously selected in both the input and the target image. However, few authors used landmarks for registration evaluation of DCE-MRI time series, probably due to the lack of reliable and locally identifiable anatomical structures [34,39]. Some have employed synthetic datasets [24,40], though it is not known whether the motion and noise patterns in the synthetic model are sufficiently close to in vivo DCE-MRI kidney data. Alternatively, other authors have used the goodness-of-fit of the time series to a smooth pharmacokinetic model before and after registration [21,34–37]. The goodness-of-fit is intrinsically linked to the smoothness of the time curves, since smoother time curves are better fitted to a smooth model. Thus, the goodness-of-fit and smoothness of time curves are frequently used criteria for successful registration evaluation of DCE-MRI data and we employ them for performance evaluation in the present work. Additionally, the measurement of physiological parameters acquired with gold-standard methods requiring blood sampling can also be used to evaluate the physiological implication of various registration methods [34]. We have therefore computed the GFR of five subjects (ten kidney data sets, two for each subject), and compared the obtained MR-GFR values to Iohexol clearance (clinical gold standard, [41]) as an additional evaluation criterion.

The major contributions of our work are the incorporation and implementation of the similarity measures NGF and MI in the deformable viscous fluid registration framework [42], together with a rigorous performance evaluation of MI and NGF for registration of kidney DCE-MRI recordings. We show that NGF and MI can be successfully applied to DCE-MRI, and to the best of our knowledge, this is the first report where the applicability and accuracy of these cost functions for co-registration of DCE-MRI time series have been thoroughly evaluated.

2. Dynamic contrast enhanced magnetic resonance imaging (DCE-MRI) of the kidney

We used a 1.5 T MR-scanner (Avanto, Siemens) to acquire image data from five healthy volunteers. All participants gave their written consent. A breath-hold T1-weighted 3D single gradient recall echo (GRE) pulse sequence was used to acquire signal-intensity time curves after administration of a small dose (2 ml) of gadolinium contrast media intravenously. The acquisition was regular during periods of breath-hold, with sampling time of either 2.85 s (subjects 1 and 5) or 2.45 s (subjects 2–4), irregular otherwise. The acquisition parameters for the two examinations are summarized in Table 1. When the injected bolus (tracer) arrives in the tissue, the MRI signal increases due to T1-shortening. The temporal changes in the signal intensity can be used to compute the concentration of the tracer. The image sequences, as functions of time, appear almost "uni-modal" outside the kidneys due to the late and slower inflow of tracer in these anatomical regions, and "multi-modal" inside the kidney. The goal is to restore the signal intensity dynamics from contrast agent wash-in and wash-out, and, at the same time, eliminate the intensity variations due to motion artifacts by a geometric correction. Examples of images at pre-contrast, at maximum contrast (cortical enhancing) and at late-contrast (pelvic enhancing) phase of the five volunteers are shown in Fig. 1.

3. Image registration – theory and numerical scheme

We consider a deformable model based on the viscous fluid registration of Christensen [42,43]. In a continuous formulation, the input image $f : \Omega \to \mathbb{R}$ is considered a viscous fluid, deforming into the reference image $g : \Omega \to \mathbb{R}$ within the image domain $\Omega \subset \mathbb{R}^3$. The registration framework is formulated in the Eulerian reference frame, where the velocity $\mathbf{v} : \mathbb{R}^3 \times \mathbb{R} \to \mathbb{R}^3$ at position $\mathbf{x}(t) \in \mathbb{R}^3$ and time $t \in \mathbb{R}$ is the material derivative of the displacement $\mathbf{u} : \mathbb{R}^3 \times \mathbb{R} \to \mathbb{R}^3$,

$$\mathbf{v}(\mathbf{x}(t), t) = \frac{\partial \mathbf{u}(\mathbf{x}(t), t)}{\partial t} + \mathbf{v}(\mathbf{x}(t), t) \cdot \nabla \mathbf{u}(\mathbf{x}(t), t). \tag{1}$$

This formulation allows for large displacements since the PDE is solved for the velocity and the total displacement is accumulated by solving (1) for $\mathbf{u}(\mathbf{x}(t), t)$. Navier's equation is solved for the velocity $\mathbf{v}(\mathbf{x}(t), t)$,

$$\mu \Delta \mathbf{v} + (\mu + \lambda) \nabla (\nabla \cdot \mathbf{v}) = \mathbf{b}(\mathbf{x} - \mathbf{u}) \tag{2}$$

where $\mathbf{b} : \mathbb{R}^3 \times \mathbb{R} \to \mathbb{R}^3$ is the force field, driving the deformation, and $\mu, \lambda \in \mathbb{R}$ are the Lamé constants. The Laplacian term $\Delta \mathbf{v}$ performs smoothing on the velocity field by constraining the velocity spatially. The term $\nabla(\nabla \cdot \mathbf{v})$ controls the contraction or expansion of

Table 1
Acquisition parameters for the DCE-MRI time series. Two acquisitions are Flash3D and the remaining are Twist with isotropic voxels.

Subject	Contrast agent	TR (ms)	TE (ms)	FA (deg)	Matrix	Type (mm^3)	Voxel size (mm)	FOV	# Time points
1	Dotarem	2.41	0.87	12	256×256	Flash3D	$1.66 \times 1.66 \times 3$	425	45
2–4	Multihance	2.51	0.89	15	256×192	Twist	$1.8 \times 1.8 \times 1.8$	460	49
5	Multihance	2.41	0.87	12	256×256	Flash3D	$1.66 \times 1.66 \times 3$	425	43

the fluid. The force field is defined as the derivative of a cost function $C(\mathbf{u})$. For an input image f and a reference image g having the same intensity range, the sum of squared differences is often used as the cost function (or similarity measure),

$$C_{SSD}(\mathbf{u}) = \frac{1}{2}\int_{\Omega} (f(\mathbf{x}-\mathbf{u}) - g(\mathbf{x}))^2 d\mathbf{x}, \tag{3}$$

taking low values as f and g become more similar on the image domain Ω.

However, for images of different modality, SSD is often inappropriate since similar intensities cannot be expected, even when the underlying structure is the same. In the past, cost functionals like correlation ratio, mutual information and normalized gradients [26] have been developed and used for this type of image registration. The DCE-MRI images recorded after the bolus injection have a time- and position-dependent signal intensity variation. Within the kidney wash-in and wash-out creates a strongly time varying and locally dependent intensity profile, highlighting edges between different kidney tissue. Yet, the geometry of the imaged organs is the same, suggesting that one should make use of spatial information. Therefore, we propose to apply normalized gradients as a similarity measure for the registration of DCE-MRI time series. Define the normalized gradients

$$\tilde{\nabla} f = \frac{\nabla f}{\sqrt{||\nabla f||^2 + \eta^2}} = \frac{\nabla f}{||\nabla_\eta f||} \tag{4}$$

and the regularized absolute gradients $||\nabla_\eta f||^2 = ||\nabla f||^2 + \eta^2$ where η is an edge parameter that controls the influence of image

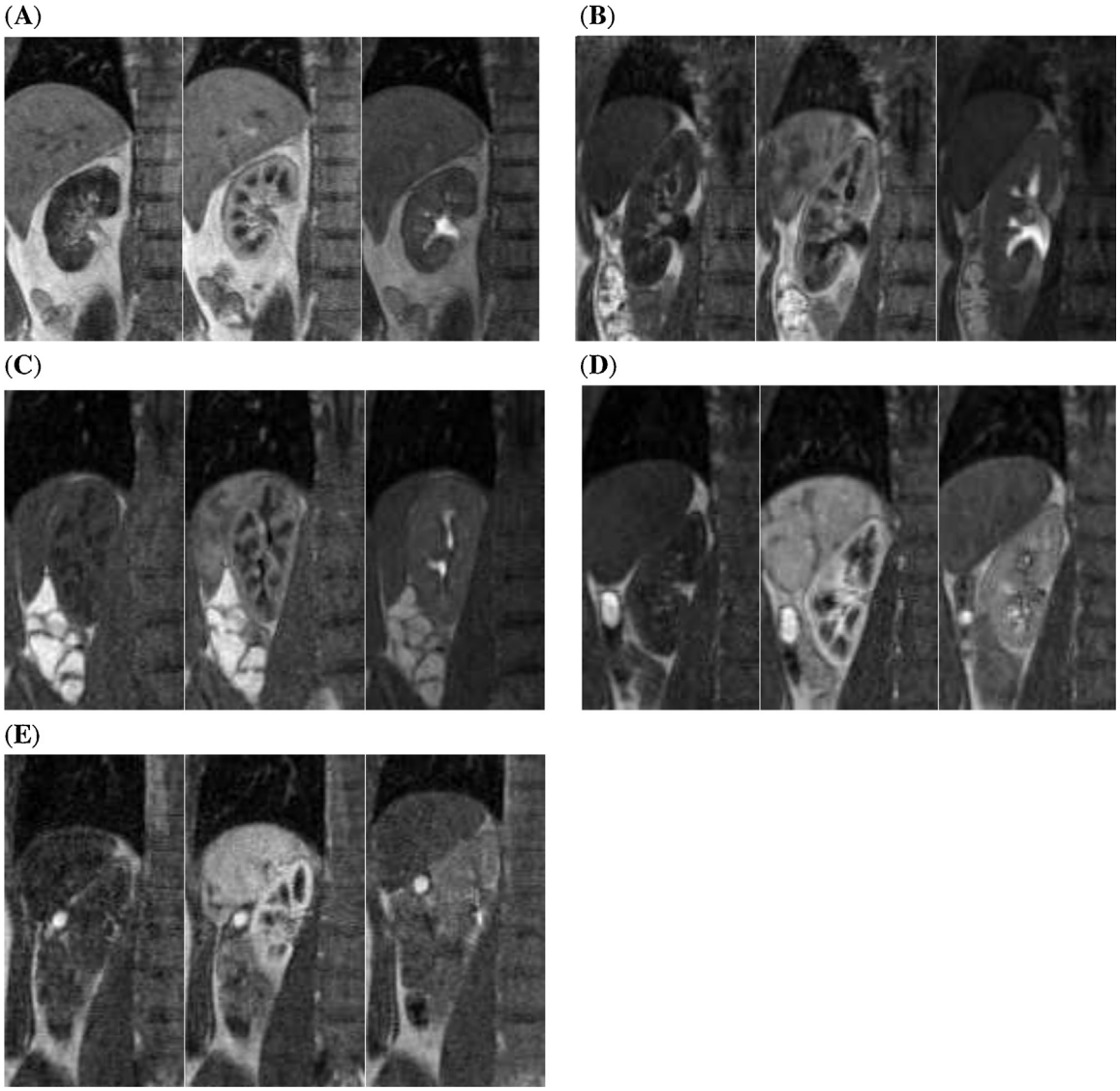

Fig. 1. Unprocessed DCE-MRI time sequences before contrast (left image), at maximal contrast enhancement, cortical phase (middle image) and late-contrast, pelvic phase (right image) for the five subjects included in the study (**A**–**E**).

gradients.[1] Typically, η should be set in the range of the edges of interest. Then, a cost function based on normalized gradients can be phrased as

$$C(\mathbf{u}) = \int_\Omega 1 - (\tilde{\nabla} f(\mathbf{x}-\mathbf{u})^T \cdot \tilde{\nabla} g(\mathbf{x}))^2 d\mathbf{x} \tag{5}$$

$$\tag{6}$$

which is minimized when the gradients are aligned or oppositely aligned, occurring at places of correlation of edges between the input and target image. This will allow for both dark to light transitions of the signal intensity, and also the opposite within the same image and for the same tissue. Now, for simplicity, let $f = f(\mathbf{x}-\mathbf{u})$ and $g = g(\mathbf{x})$. Then, the force field, can be written as

$$\mathbf{b}_{ngf} = \frac{\partial C}{\partial \mathbf{u}} = \frac{2(\tilde{\nabla} f^T \tilde{\nabla} g) H(f)}{||\nabla_\eta f||} \left[\tilde{\nabla} g - (\tilde{\nabla} f^T \tilde{\nabla} g)\tilde{\nabla} f\right] \tag{7}$$

where $\mathbf{H}(f)$ is the Hessian of $f(\mathbf{x}-\mathbf{u})$,

$$H_{ij}(f) = \frac{\partial^2 f(\mathbf{x}-\mathbf{u})}{\partial x_i \partial x_j}. \tag{8}$$

For fluid registration using normalized gradients, the equation to solve for $\mathbf{v}$ becomes

$$\mu \Delta \mathbf{v} + (\mu + \lambda)\nabla(\nabla \cdot \mathbf{v}) = \mathbf{b}_{ngf} \tag{9}$$

in combination with a time evolution of (1).

3.1. Combining transformations into a global transformation

In the registration process, the transformation can in principle become singular (i.e. the determinant of the Jacobian becomes zero or negative). In this case, a regridding of the image and resetting of the transformation to $\mathbf{u} = 0$ is necessary. Usually, this is performed by applying the current transformation to the image by interpolation so that a "new" image is created for further iterations. Upon several regrids, this process will deteriorate the image, due to interpolation effects. Therefore, it is desirable to act only on the transformation, and not on the image. We achieve this by combining the obtained transformations into a single global transformation [42], which requires only a single regrid (the final) of the image. This concatenation of transformation fields is also useful for multiscale registration where the propagation of the transformation field from one scale to another is required. Let $f = f^{(0)}$ be the input image. When the transformation becomes close to singular (from now on called regrids) the transformed image is defined as

$$f^{(1)}(\mathbf{x}) = f^{(0)}(\mathbf{x} - \mathbf{u}^{(1)}(\mathbf{x})) \tag{10}$$

This formula is valid between each level $j = 1, \ldots, n$, as long as $\mathbf{x}$ is the grid of the current level. Define $\mathbf{a}^{(n)} = \mathbf{x}$ which is the grid of transformation n. From level n to level $n-1$ replace $\mathbf{x} \mapsto \mathbf{x} - \mathbf{u}$. Then, the desired globally transformed image $f^{(n)}$ can be expressed as a function of $f^{(0)}$ recursively

$$\begin{aligned} f^{(n)}(\mathbf{x}) &= f^{(n-1)}(\underbrace{\mathbf{a}^{(n)} - \mathbf{u}^{(n)}(\mathbf{a}^{(n)})}_{\mathbf{a}^{(n-1)}}) \\ &= f^{(n-2)}(\underbrace{\mathbf{a}^{(n-1)} - \mathbf{u}^{(n-1)}(\mathbf{a}^{(n-1)})}_{\mathbf{a}^{(n-2)}}) \\ &= \ldots \\ &= f^{(0)}(\underbrace{\mathbf{a}^{(1)} - \mathbf{u}^{(1)}(\mathbf{a}^{(1)})}_{\mathbf{a}^{(0)}}), \end{aligned} \tag{11}$$

which results in

$$\mathbf{a}^{(j-1)} = \mathbf{a}^{(j)} - \mathbf{u}^{(j)}(\mathbf{a}^{(j)}). \tag{12}$$

By computing $\mathbf{a}^{(0)}$ the global deformation $\mathbf{u}_g(\mathbf{x})$ can be found from $\mathbf{x} - \mathbf{u}_g(\mathbf{x}) = \mathbf{a}^{(0)}(\mathbf{x})$ and applied to the original image $f^{(0)}$. In our experiments, it never occurred that the transformation became singular, although the method allows for it. We used (12) to combine transformation fields from different multiscale levels.

3.2. Numerical implementation

The Euler equation (1) is discretized by a forward Euler scheme,

$$\mathbf{u}[\mathbf{x}, t_{i+1}] = \mathbf{u}[\mathbf{x}, t_i] + \delta t(\mathbf{I} - \nabla \mathbf{u}[\mathbf{x}, t_i])\mathbf{v}[\mathbf{x}, t_i] \tag{13}$$

$$= \mathbf{u}[\mathbf{x}, t_i] + \delta t \nabla \mathbf{r}[\mathbf{x}, t_i]\mathbf{v}[\mathbf{x}, t_i] \tag{14}$$

where $\delta t = t_{i+1} - t_i$. (h_1, h_2, h_3) is the voxel size, (n_1, n_2, n_3) is the number of voxels in the regular image grid in the respective directions $\mathbf{x} = (x_1, x_2, x_3)$ and $\nabla \mathbf{r}$ is labelled as the transformation.

In [44,45] the speed $\mathbf{v}$ was defined as the convolution of the force field with a Gaussian spatial smoothing kernel Ψ,

$$\mathbf{v} = \Psi(\mathbf{x}) \otimes \mathbf{b}(\mathbf{x}, \mathbf{u}). \tag{15}$$

However, we have not followed this approach since Bro-Nielsen et al. [43] claim that this approximation can possibly give problems in terms of topology and stability of the fluid model. Instead, we solve Navier's equation (2) in the Fourier domain. This creates an easy system to solve, which also saves considerably memory compared to solving a large system of linear equations simultaneously [46]. Deformable, non-parametric image registration in the Fourier domain has previously been reported [47,48]. In Fourier basis, the velocity $\mathbf{v}$ can be written as

$$\begin{aligned} \mathbf{v}(\mathbf{x}) &= \int_\Omega \mathbf{w}(\tilde{\mathbf{k}}) e^{2\pi i(\tilde{\mathbf{k}}^T \cdot \mathbf{x})} d\mathbf{k},\ \Omega \\ &= \{\mathbf{x} \ \mid \ x_i \in [-K_i/2, K_i/2] \ \ \forall \ \ i = 1, 2, 3\} \end{aligned} \tag{16}$$

where $\tilde{\mathbf{k}} = \left(\tilde{k_1}, \tilde{k_2}, \tilde{k_3}\right)^T = \left(\frac{k_1}{K_1}, \frac{k_1}{K_2}, \frac{k_3}{K_3}\right)^T$. Thus, K_i is the length of Ω in each main direction. The discretized counterpart is

$$\mathbf{v}[\mathbf{x}] = \sum_{\tilde{\mathbf{k}}} \mathbf{w}_{\tilde{\mathbf{k}}} e^{2\pi i(\tilde{\mathbf{k}}^T \cdot \mathbf{x})} \tag{17}$$

where $K_i = n_i h_i$ is the length of the image domain in direction i and $k_i = (-K_i/2, -K_i/2 + h_i, \ldots, K_i/2)^T$ is the coefficients in the Fourier domain. Upon differentiation the Laplace term becomes

$$\Delta \mathbf{v} = -(2\pi)^2 \sum_{\tilde{\mathbf{k}}} \mathbf{w}_{\tilde{\mathbf{k}}} (\tilde{\mathbf{k}}^T \cdot \tilde{\mathbf{k}}) e^{2\pi i(\tilde{\mathbf{k}}^T \cdot \mathbf{x})} \tag{18}$$

and the advection term can be written as

$$\nabla(\nabla \cdot \mathbf{v}) = -(2\pi)^2 \sum_{\tilde{\mathbf{k}}} \mathbf{w}_{\tilde{\mathbf{k}}} (\tilde{\mathbf{k}} \cdot \tilde{\mathbf{k}}^T) e^{2\pi i(\tilde{\mathbf{k}}^T \cdot \mathbf{x})}. \tag{19}$$

The right hand side, the force term, we express as

$$\mathbf{b}_{ngf} = \sum_{\tilde{\mathbf{k}}} \mathbf{r}_{\tilde{\mathbf{k}}} e^{2\pi i(\tilde{\mathbf{k}}^T \cdot \mathbf{x})}. \tag{20}$$

Thus, using (9), the system to solve for each voxel becomes

$$-(2\pi)^2 A \mathbf{w}_{\tilde{\mathbf{k}}} = \mathbf{r}_{\tilde{\mathbf{k}}} \tag{21}$$

where

$$A = \mu \tilde{\mathbf{k}}^T \tilde{\mathbf{k}} I + (\mu + \lambda)\tilde{\mathbf{k}}\tilde{\mathbf{k}}^T. \tag{22}$$

[1] In [29] it was claimed, but not proved, that for equation (4) the gradients may evaluate to nonzero even in a global minimum due to numerical approximations.

The matrix A is real and symmetric and is therefore self-adjoint, thus $A^* = A$. Since A is essentially a rank-one perturbation of the identity, A is singular only if $\tilde{k_1} = \tilde{k_2} = \tilde{k_3} = 0$, corresponding to the zero frequency. This implies that the solution for the zero frequency need not exist, or, if it exists, there are infinitely many solutions. In the operator setting, this is referred to as *Fredholm alternative*. To overcome this problem, we impose an even number of voxels in at least one spatial direction of high resolution, and consider an interpolation of the differential operator on that grid, that is staggered with respect to that of the theoretical differential operator. This is equivalent to introducing a tiny phase shift to the functions in the Fourier domain. The operator is not discretized exactly on the original function, but on a slightly different grid. The advantage is that the staggered operator is now nonsingular, and therefore we can solve for all the unknowns, and a unique solution is guaranteed.

The advantage of solving Navier's equation in the Fourier domain is obvious since this is only a 3×3 linear system which is easily solved using a small amount of memory. Alternatively, using an implicit approach with standard divided-differences would require the storage of huge, albeit sparse matrices. Furthermore, the Fourier approach is much easier to set up than the implicit approach with respect to the creation of the large matrix of divided differences, and it is favorable to implement in parallel, for instance on the GPU. In practice, we solve the small linear system by LU decomposition, thus obtaining a fast and accurate solver using little computer memory. In order to improve the speed and also to allow large displacements we implemented the fluid registration as a multilevel scheme. The levels are organized as scaling by a user-defined parameter $\boldsymbol{\alpha} = (\alpha_1, \alpha_2, \ldots, \alpha_p), \alpha_i \in [0, 1]$. Let $f_{[i]}^{(0)}$ be the initial image at level i. In order to pass the global displacement field $\mathbf{u}_{g,[i]}$ from level i to $i+1$, the global transformation $\mathbf{u}_{g,[i]}$ from the previous level is passed to the next by interpolation, thus computing $f_{[i+1]}^{(1)}(\mathbf{x}) = f_{[i+1]}^{(0)}(\mathbf{x} - \mathbf{u}_{g,[i]})$. If the Jacobian (Jacobian determinant) of the transformation $\nabla\mathbf{r}$ drops below the given threshold, the obtained transformation is concatenated onto the global transformation $\mathbf{u}_{g,[i+1]}$ and $f_{[i+1]}^{(2)}(\mathbf{x}) = f_{[i+1]}^{(1)}(\mathbf{x} - \mathbf{u}_{g,[i+1]})$ is computed. In other words, we *always operate on the grid* and we apply at most one final regrid to the image. Practically, for in our experiments here, we stop iterating when the transformation has a Jacobian less than 0.4 in order to avoid singularities. Convergence of the cost functional was reached before the limit of 0.4 was exceeded.

The iterations on a given level are terminated if the maximum number of iterations has been reached, if the cost functional is non-decreasing over several iterations, or if the force term drops below a certain value, specifically if

$$||\mathbf{b}||_{L2} = \sqrt{\left(\sum_i (b_i(\mathbf{x}, \mathbf{u}))^2\right)} < T \tag{23}$$

where T is a user-defined threshold. The registration scheme is organized as follows:

A. Preprocessing:

1. Set up the grids in natural coordinates with the origin in the center of the image.
2. Set up the multilevel hierarchy for p levels, where p is the finest level. The input image f, reference image g and the grids X, Y, Z are resized to $\alpha_i \in (0, 1]$, which is the multilevel parameter. After resizing, the number of voxels will be $\alpha_i(n_x \times n_y \times n_z)$ for level i.
3. The affine displacement $\mathbf{u}_A$ is computed using FSL's FLIRT [49].
4. The affine displacement $\mathbf{u}_A$ is given as argument to the fluid registration.
5. The coefficient matrix A is computed for each level. Multilevel is set to $i = 1$ at α_i (the coarsest grid).

B. Multilevel:

1. Iterate on level i: $\mathbf{u}_g$ is taken as the affine registration or from the previous level (interpolated) of the fluid registration. Compute $f_{[i]}^{(1)}(\mathbf{x}) = f_{[i]}^{(0)}(\mathbf{x} - \mathbf{u}_g)$ and set $\mathbf{u} = 0$.
   (a) Compute the force $\mathbf{b}_{ngf}$ using (7).
   (b) Perform Fourier transform of the force, (20). Solve (21) for $\mathbf{w}_{\tilde{\mathbf{k}}}$, the Fourier coefficients. Apply inverse Fourier transform to obtain the velocity $\mathbf{v}$ (17).
   (c) Choose a time step δt such that every element of the flow $\delta t \nabla \mathbf{r}(\mathbf{x}, t) \cdot \mathbf{v}(\mathbf{x}, t)$ is less than a maximal flow. In our code we have used global settings for this parameter, equal to 0.01. If this is not satisfied for all points, δt is halved until the condition is satisfied. Update $\mathbf{u}$ by (14).
   (d) If the Jacobian $|\nabla \mathbf{r}| < 0$, the transformation in (14) becomes ill-conditioned. In our code, we would regrid if $|\nabla \mathbf{r}| < 0.4$. The global transformation $\mathbf{u}_g$ is computed by concatenating the global transformation of the previous level with the transformations of the current level according to (12), and the current transformation is reinitialized as $\mathbf{u} = 0$.
   (e) Stop iterating if the maximum number of iterations has been reached, if the cost functional is non-decreasing, or if the force goes to zero, $||\mathbf{b}||_{L_2} < T$ (23).
2. If level $i < p$, proceed to next level, $i = i + 1$, thus go to step B1, else go to step B3.
3. Resample image according to the obtained $\mathbf{u}_{g,[p]}$ on the finest level p by computing $f(\mathbf{x} - \mathbf{u}_{g,[p]})$.

4. Mutual information

To perform a fair comparison of the similarity measures, MI [30,31] was also implemented in the fluid registration framework, as described in [44,45,50]. This implementation was done in order to remove the influence of the deformation model on the results. Mutual information is defined as

$$MI = \sum_{i_1}\sum_{i_2} p(i_1, i_2) \log \frac{p(i_1, i_2)}{p(i_1)p(i_2)} \tag{24}$$

where $p(i_1, i_2), p(i_1), p(i_2)$ are joint and marginal intensity probability distributions, and i_1, i_2 are the intensities of the input and target image, respectively. The joint and marginal probabilities were evaluated using a Parzen window,

$$p(i_1, i_2) = \frac{1}{V} \int_\Omega \psi(i_1 - f(\mathbf{x} - \mathbf{u}), i_2 - g(\mathbf{x}))dx \tag{25}$$

where V is the volume of Ω and ψ is a 2D Gaussian convolution kernel

$$\psi(i_1 - f(\mathbf{x} - \mathbf{u}), i_2 - g(\mathbf{x})) = \frac{1}{(2\pi)^{k/2}|\Sigma|^{1/2}} e^{-\frac{1}{2}\tilde{\mathbf{x}}^T \Sigma^{-1} \tilde{\mathbf{x}}} \tag{26}$$

with Σ as the sample covariance matrix and $\tilde{\mathbf{x}} = (i_1 - f(\mathbf{x} - \mathbf{u}), i_2 - g(\mathbf{x}))^T$. The MI gradient, used as the force in fluid registration, is given by a convolution

$$\mathbf{b}_{MI} = \nabla MI = \frac{1}{V}\left(\frac{\partial \psi}{\partial i_1} * L(i_1, i_2)\right) \nabla f(\mathbf{x} - \mathbf{u}) \tag{27}$$

with

$$L(i_1, i_2) = 1 + \log \frac{p(i_1, i_2)}{p(i_1)p(i_2)}. \tag{28}$$

The convolution is with respect to the entire intensity space $\mathbb{R}^2$.

5. Registration evaluation

A proper evaluation of multi-modal image registration can be challenging due to the lack of a ground truth for real images. We have chosen to be in line with other DCE-MRI studies using the smoothness of the time curves as well as the deviation between the data and the solution of a smooth compartment model. These approaches have been adopted in several relevant publications [21,34–37]. The smoothness of time curves and the deviation to a compartment model are strongly linked since smooth time curves will contribute to lower deviation between the data and a compartment model. Poorly registered data will contribute to more oscillatory behavior of voxel time courses, which will affect these two measurements for registration performance. Moreover, from the compartment modeling, we have computed a physiological relevant parameter for each subject, the GFR. We compare the obtained MR-GFR with Iohexol GFR, which is considered a gold standard for GFR measurements in the clinic. From these two GFR estimations we can judge about the physiological relevance of the registration method of choice. The approach for compartment modelling is described below.

5.1. Compartment modeling

As described in [51,52], a two-compartment model for kidney filtration can be defined for the plasma and tubular compartments. Given the normalized tracer concentration in the arterial, plasma and tubular compartments as C_a, C_p and C_t, the plasma concentration can be expressed as

$$C_p(t) = \frac{1}{T_p}\int_0^t C_a(\tau)e^{-(t-\tau)/T_p}d\tau \tag{29}$$

where T_p is the mean transit time for the plasma compartment. The temporal change of tracer in the tubular compartment is assumed to be proportional to the difference in concentration across the filtration barrier, such that

$$V_t\frac{dC_t(t)}{dt} = F_tC_p(t) - (1-f)F_tC_t(t) \tag{30}$$

where F_t is the GFR and $(1-f)F_t$ is the output of the tubular compartment. Solving (30) for $C_t(t)$ and summing up the total tracer as $C = V_pC_p + V_tC_t$ results in

$$C(t) = V_pC_p(t) + F_t\int_0^t C_p(\tau)e^{-(t-\tau)/T_t}d\tau \tag{31}$$

where $C(t)$ is the contrast agent concentration and

$$T_t = \frac{V_t}{F_t(1-f)}. \tag{32}$$

More details regarding the applied compartment model can be found in [51] and [52].

For an overall evaluation of the registration performance, the average root-mean-square (RMS) value between the observed time curves and the model time curves was computed. This method for evaluation assumes that better registered data will provide smaller distances between the observed data and the model curve. Specifically, the distance between the observable concentration $C_o(t)$ and the model concentration $C(t)$ was computed for every voxel within the kidney (S). For a given voxel x, let $c_o(x,t) = C_o(t)$ and let $c(x,t) = C(t)$ as from (31). Then,

$$RMS(x) = \sqrt{\frac{1}{T}\sum_{t=t_1}^{T}(c_o(x,t) - c(x,t))^2} \tag{33}$$

with the average RMS value ($\overline{RMS}$)

$$\overline{RMS} = \frac{1}{|S|}\sum_{x\in S}RMS(x), \tag{34}$$

used as performance measure for registration within the kidney volume S.

5.2. Renal segmentation for compartment modeling

To estimate the single-kidney GFR, a renal segmentation was applied to the kidney as a whole. For segmentation, we used the Mahalanobis distance, a higher dimensional distance measure between the time curves of voxels and the time curves of manually given training masks grouping of the voxels into a two-phase segmentation. The training masks were coarsely, manually labelled in 2D prior to segmentation, and the time curves from these voxels were assembled into a matrix $Y_{N\times T}$ where N is the number of voxels in the training mask, and T is the number of time steps in the time series. Such training set was processed twice, providing one training set for the kidney (Y_1), and another one for the background (Y_2). Given a vector y with temporal elements

$$y_i = f(x,t_i), \tag{35}$$

for any position x, the squared Mahalanobis distance from y to a training set Y is a vector-matrix-vector product and can be written as a double sum

$$d(y,Y)^2 = \sum_{i=1}^{T}\sum_{j=1}^{T}(y_i-\mu_i)S^+_{i,j}(y_j-\mu_j). \tag{36}$$

Here, $S = \mathrm{covar}(Y)$ over the columns of Y, and S^+ is the Moore-Penrose pseudoinverse matrix. The average μ_i for a timepoint i is

$$\mu_i = \frac{1}{N}\sum_{j=1}^{N}Y_{j,i}. \tag{37}$$

Equation (36) gives the squared Mahalanobis distance between a T-dimensional feature vector y to the set Y, reflecting both the orientation of Y and its average. The segmentation is obtained as the phase with the minimum Mahalanobis distance to the corresponding training mask

$$\mathrm{argmin}_i d(y(x), Y_i). \tag{38}$$

The training masks are manually drawn in 2D on the reference image. They do not require accurate delineation, but each training mask must include the intended tissue types belonging to the phase. The total GFR was computed by multiplying single-kidney GFR with the respective kidney volume, and then adding the resulting left and right values. The five subjects GFR values are reported in Table 4.

5.3. Temporal variation

As an additional evaluation criterion, the temporal variation of signal intensity time curves was computed within the kidney S as

$$d = \frac{1}{T|S|}\int_0^T\left(\int_S\left|\frac{\partial f}{\partial t}\right|dx\right)dt, \qquad T>0, \tag{39}$$

with f as the image arising from different registration methods. The temporal variation was restricted to the kidney since this is the region of interest for GFR estimations. A discrete version of (39) was used.

5.4. Estimation of Gadolinium concentration

For the GFR calculations, the voxel wise Gadolinium concentration had to be estimated from the DCE-MRI time series. We adopted the approach in [53] by estimating pre-contrast T_1 times, here referred to as T_{10}. A linear model was fitted to

$$\frac{S_i}{\sin\alpha_i} = m\frac{S_i}{\tan\alpha_i} + M_0(1-m), \tag{40}$$

where S_i is the measured signal for flip angle α_i, $i = 1, 2, \ldots$, and M_0 is the equilibrium magnetization of 1.5T. T_{10} can be derived from the slope $m = \exp(-TR/T_{10})$. The relaxation R_{10} relates to T_{10} by $R_{10} = 1/T_{10}$. For low gadolinium concentrations (0–5 mM) we have imposed the assumption

$$R_1 = R_{10}\frac{s}{s_0}, \tag{41}$$

according to [54], given the precontrast and contrast signal intensities s_0, s, respectively. Additionally, there is an linear relationship between the gadolinium concentrations and the relaxation R_1,

$$R_1 = R_{10} + r_1 C, \tag{42}$$

valid in regime of low tracer concentrations. Here, r_1 is the relaxivity of the tracer and C is the gadolinium concentration that we want to estimate [16]. We used $r_1 = 4.1\,\mathrm{mM}^{-1}\,\mathrm{s}^{-1}$ for Multihance and $r_1 = 4.3\,\mathrm{mM}^{-1}\,\mathrm{s}^{-1}$ for Dotarem [55].

6. Results

In this section we compare the performance of NGF with unprocessed images, affine registration and mutual information (MI). NGF as well as MI were both applied within the same fluid registration framework to rule out possible differences arising from the deformation model. For reproducibility and easy parameter tuning of η, all images were scaled to [0, 1] prior to fluid registration. After registration, the obtained transformation was applied to the original images to recover the original intensity range.

6.1. NGF creates smoother time intensity curves

We computed the temporal variation (39) from ten kidney data sets, two kidneys (left and right) for each of the five subjects. The results are reported in Table 2. NGF had the lowest temporal variation and MI had the second lowest for all ten data sets. Affine registration had lower temporal variation than unprocessed images in all data sets except from two data sets, and unprocessed images had the highest variation in the remaining data sets.

Table 2
Average temporal variation (39) for left (l) and right (r) kidney in unprocessed images, affine, NGF, and MI. NGF has lowest temporal variation in each data set as well as in average over all data sets. Units are in signal intensities. Asterisks indicate best values.

Subject/l,r	Unprocessed	Affine	NGF	MI
1/l	3.72	3.25	2.89*	2.94
1/r	4.10	3.40	3.01*	3.11
2/l	2.53	2.34	2.14*	2.28
2/r	2.97	2.85	2.76*	2.84
3/l	2.12	1.92	1.79*	1.81
3/r	2.08	1.96	1.82*	1.86
4/l	3.29	3.34	3.15*	3.19
4/r	2.66	2.67	2.50*	2.52
5/l	4.91	3.96	3.47*	3.60
5/r	4.75	4.13	3.57*	3.66
Average	3.31	2.98	2.71*	2.78

Table 3
Average deviation to the compartment model for left (l) and right (r) kidney in unprocessed images, affine, NGF, and MI. The average deviation to the compartment model over all data sets is lowest for NGF. Units are in signal intensity values. Asterisks indicate best values.

Subject/l,r	Unprocessed	Affine	NGF	MI
1/l	58.4	48.8	39.4*	42.6
1/r	84.1	61.5	57.9	56.2*
2/l	47.8	45.7	40.6*	46.0
2/r	42.3	42.5	42.5	36.7*
3/l	80.1	51.9	21.6*	34.9
3/r	138.9	84.8	33.7*	50.4
4/l	47.6	27.0	21.0*	28.9
4/r	21.3	20.2	15.9*	17.7
5/l	133.7	96.8	88.2*	96.3
5/r	123.6	177.7	95.4	61.1*
Average	77.8	65.7	45.6*	47.1

Table 4
Average deviation of total MR-GFR (ml/min) to Iohexol GFR using various registration methods and the compartment model in (31). The NGF cost function gives on overall the best estimation of GFR as compared to Iohexol GFR.

Subject	Unprocessed	Affine	NGF	MI	Iohexol
1	58.78	90.53	112.89	54.42	101.00
2	50.71	51.03	69.63	60.11	94.00
3	167.80	106.95	99.26	105.21	127.00
4	74.06	94.05	108.89	81.21	106.00
5	62.95	89.04	91.16	90.65	94.00
$\overline{d}_{gfr}$	37.86	18.08	13.95	26.08	–

6.2. NGF has a lower deviation to a fitted compartment model

We found that NGF had the lowest deviation (34) between the Gadolinium concentration time curves and the fitted compartment model (31) for seven out of ten data sets (cfr. Table 3). MI had the lowest deviation in three data sets. Unprocessed images had the largest deviation in nine experiments and affine registration had the largest deviation in two data sets. NGF had the lowest average deviation, followed by MI with the second lowest deviation.

6.3. NGF has the best GFR estimate compared to Iohexol clearance

We used the compartment model in (31) applied to the Gd concentration time curves in order to estimate the MR-GFR in all five subjects. The GFR was also estimated by clearance of Iohexol, used as a reference method. The method of Iohexol clearance is restricted to *total* GFR, entailing both left and right kidney. The results are presented in Table 4, the last column containing Iohexol GFR measurements. The estimated $\overline{d}_{gfr}$ was computed as the absolute value of the difference between MR-GFR and Iohexol GFR, and then averaged across all subjects. For three out of five subjects NGF had the lowest deviation to Iohexol measurements, and MI and affine registration had the lowest deviation for one subject each. On average, NGF had the lowest deviation, followed by affine registered images, MI and unprocessed images with the largest deviation.

7. Discussion and conclusions

Image registration is an increasingly important and often challenging image processing task with a broad range of medical applications. In this paper we proposed the use of normalized gradient fields (NGF) [28] as a similarity measure for DCE-MRI, combined with a deformable fluid registration [42]. The performance of NGF was tested against MI within the same deformable fluid registration framework. The driving application is the goal of estimating voxel-wise glomerular filtration rate (GFR) from motion-corrected

time courses of DCE-MRI of the kidney. We applied three evaluation criteria, (i) smoothness of time curves, (ii) deviation to a fitted compartment model and (iii) deviation of estimated GFR values from Iohexol measurements. For evaluation criteria (i) and (ii) we found that, on average, unprocessed images had the poorest performance, followed by affine registration, MI and NGF in increasing order. These results show that both MI and NGF improve the registration quality of the time series. For the estimated GFR, we found the best performance of NGF, followed by affine registration. This indicates that NGF improved the ability to estimate physiological parameters from the recorded data, compared to unprocessed, affine registered data, as well as MI registered data.

Insofar a direct comparison of NGF and MI is concerned, we found that with respect to (i), NGF improved the temporal smoothness more consistently than MI across all ten data sets. For (ii), NGF had better performance in seven out of ten data sets, MI in three out of ten data sets. With respect to the GFR estimations (iii), NGF had the best performance in three out of five data sets, MI in two out of five data sets. The average deviation to Iohexol GFR was substantially lower for NGF than MI. Also visual inspection revealed a less oscillatory temporal signal intensity pattern in NGF compared to the other conditions. This observable discrepancy between NGF and MI for co-registration of kidney DCE-MRI time courses can probably be explained by the nonuniform change of signal intensities upon bolus arrival, which creates a more dispersed joint histogram for MI. The three quantitative evaluation criteria as well as visual inspection indicate that NGF has better performance than MI on DCE-MRI data sets of kidney. Although experimental data are sparse, hindering a rigorous statistical analysis, our results indicate that both NGF and MI perform well in co-registration of DCE-MRI images, with an additional improvement of NGF compared to MI. NGF could therefore be considered in further development and testing towards clinial applicability as an alternative to MI. This result is of particular interest in the light of previous DCE-MRI studies [20–23], in which MI was the similarity measure of choice.

The robustness and versatility of any automated method depends on the demand for parameter tuning. If a component of the algorithm requires user intervention in terms of parameter specification and tuning for every pair of images within an application, it represents a large amount of effort and it might also assume deeper insight into the peculiarities of the algorithm and the given data. Thus, it is desirable to use methods that perform well with either fixed or automatically defined parameter settings. For NGF, there is essentially one parameter to tune, the edge parameter η. In our experiments, a fixed $\eta = 0.03$ was successfully applied for all examinations. Further extensive validation and testing of the NGF registration (data not shown) has revealed a global setting of $\eta = 0.03$ as suitable. This indicates that NGF, within the fluid registration framework, represents a robust approach with only a minimum of user-intervention that integrates well with an automated processing chain. Mutual information has essentially no parameters to tune, which makes it very flexible but potentially less accurate in certain situations.

Processing speed is important in many applications, and probably the most time critical registration occurs when the task is to integrate real-time images for an immediate diagnostic or therapeutic decision. In our MATLAB implementation, registration of a full DCE-MRI sequence (typically $170 \times 120 \times 26 \times 100$) requires 3–4 h of computing time on a Linux workstation with an Intel Core^{TM} i7 CPU at 2.67 GHz and 24 Gb memory, which implies that a registration would be executed and results provided within the next day in a clinical setting. Probably, a faster algorithm would increase the clinical applicability. Clearly, we have a potential for speeding up the algorithm by converting it into compiled code (e.g. MEX), by parallelizing it (e.g. CUDA) and probably also by replacing the forward Euler scheme by more robust methods that can handle larger time steps.

Future research on motion correction for DCE-MRI time series, along the idea of NGF, is to find additional image features based on geometric information that are invariant upon bolus arrival and contrast enhancement. A set of such force fields can be incorporated as a weighted combination into a common functional. Thus, one could obtain a mechanism in which different force fields are functional in various parts of the image having different geometrical information, and thereby a more robust registration method can be achieved.

In conclusion, we have shown that both normalized gradient fields and mutual information can be used in motion correction of DCE-MRI time series, with less motion artifacts compared to no registration and affine registration. However, NGF seems to perform better than MI for the DCE-MRI registration task. By these experiments, we have demonstrated that NGF is a high quality alternative to MI for image registration of DCE-MRI recordings, which are increasingly important in clinical diagnostics and therapy follow-up.

Authors contributions

EH participated in the idea, planning, programming, data analysis and performance evaluation, and writing the report. AL participated in planning and writing the report. JR participated in image recordings and writing the report. AM-K participated in the idea, planning, programming, and writing the report. All authors read and approved the final manuscript.

Acknowledgements

This work was financed by the Norwegian Research Council (NFR), project number 191178/V30. The authors want to thank Erling Andersen and Jan Anker Monssen for preprocessing and providing image data for the project.

References

[1] Fischer B, Modersitzki J. Ill-posed medicine – an introduction to image registration. Inverse Probl 2008;24(3):1–16.
[2] Birn RM, Murphy K, Bandettini PA. The effect of respiration variations on independent component analysis results of resting state functional connectivity. Hum Brain Mapp 2008;29(7):740–50, http://dx.doi.org/10.1002/hbm.20577.
[3] Damoiseaux JS, Beckmann CF, Arigita EJS, Barkhof F, Scheltens P, Stam CJ, et al. Reduced resting-state brain activity in the "default network" in normal aging. Cereb Cortex 2008;18(8):1856–64, http://dx.doi.org/10.1093/cercor/bhm207.
[4] Filippini N, Zarei M, Beckmann CF, Galluzzi S, Borsci G, Testa C, et al. Regional atrophy of transcallosal prefrontal connections in cognitively normal APOE epsilon4 carriers. J Magn Reson Imaging 2009;29(5):1021–6, http://dx.doi.org/10.1002/jmri.21757.
[5] Bucki M, Chassat F, Galdames F, Asahi T, Pizarro D, Lobo G. Real-time spect and 2D ultrasound image registration. Med Image Comput Comput Assist Interv 2007;10(Pt 2):219–26.
[6] Fei B, Flask C, Wang H, Pi A, Wilson D, Shillingford J, et al. Image segmentation, registration and visualization of serial MR images for therapeutic assessment of polycystic kidney disease in transgenic mice. Conf Proc IEEE Eng Med Biol Soc 2005;1:467–9, http://dx.doi.org/10.1109/IEMBS.2005.1616448.
[7] Dillenseger JL, Guillaume H, Patard JJ. Spherical harmonics based intrasubject 3-d kidney modeling/registration technique applied on partial information. IEEE Trans Biomed Eng 2006;53(11):2185–93, http://dx.doi.org/10.1109/TBME.2006.883653.
[8] Suh JW, Wyatt CL. Deformable registration of supine and prone colons for computed tomographic colonography. J Comput Assist Tomogr 2009;33(6):902–11, http://dx.doi.org/10.1097/RCT.0b013e3181a7e2c1.
[9] Alterovitz R, Goldberg K, Kurhanewicz J, Pouliot J, Hsu IC. Image registration for prostate MR spectroscopy using modeling and optimization of force and stiffness parameters. Conf Proc IEEE Eng Med Biol Soc 2004;3:1722–5, http://dx.doi.org/10.1109/IEMBS.2004.1403517.
[10] Alterovitz R, Goldberg K, Pouliot J, Hsu ICJ, Kim Y, Noworolski SM, et al. Registration of MR prostate images with biomechanical modeling and nonlinear parameter estimation. Med Phys 2006;33(2):446–54.

[11] Yim Y, Hong H, Shin YG. Deformable lung registration between exhale and inhale ct scans using active cells in a combined gradient force approach. Med Phys 2010;37(8):4307–17.
[12] Janssens G, Jacques L, de Xivry JO, Geets X, Macq B. Diffeomorphic registration of images with variable contrast enhancement. Int J Biomed Imaging 2011;2011:1–16, http://dx.doi.org/10.1155/2011/891585.
[13] Dey D, Ramesh A, Slomka PJ, Nakazato R, Cheng VY, Germano G, et al. Automated algorithm for atlas-based segmentation of the heart and pericardium from non-contrast CT. Proc SPIE 2010;7623:1–9, http://dx.doi.org/10.1117/12.844810.
[14] Mansi T, Pennec X, Sermesant M, Delingette H, Ayache N. Logdemons revisited: consistent regularisation and incompressibility constraint for soft tissue tracking in medical images. Med Image Comput Comput Assist Interv 2010;13(Pt 2):652–9.
[15] Zikic D, Sourbron S, Feng X, Michaely HJ, Khamene A, Navab N. Automatic alignment of renal DCE-MRI image series for improvement of quantitative tracer kinetic studies. In: SPIE Medical Imaging; vol. 6914. 2008. p. 691432–40.
[16] Sourbron S. Technical aspects of MR perfusion. Eur J Radiol 2010;76(3):304–13, http://dx.doi.org/10.1016/j.ejrad.2010.02.017.
[17] Lee VS, Rusinek H, Noz ME, Lee P, Raghavan M, Kramer EL. Dynamic three-dimensional MR renography for the measurement of single kidney function: initial experience. Radiology 2003;227(1):289–94, http://dx.doi.org/10.1148/radiol.2271020383.
[18] Sun Y, Moura JMF, Ho C. Subpixel registration in renal perfusion MR image sequence. In: IEEE International Symposium on Biomedical Imaging: Nano to Macro, 2004, vol. 1. 2004. p. 700–3.
[19] El-Baz A, Farag A, Fahmi R, Yuksela S, El-Ghar M, Eldiasty T. Image analysis of renal DCE MRI for the detection of acute renal rejection. In: 18th International Conference on Pattern Recognition, 2006. ICPR 2006, vol. 3. 2006. p. 822–5.
[20] Zöllner FG, Sance R, Rogelj P, Ledesma-Carbayo MJ, Rørvik J, Santos A, et al. Assessment of 3D DCE-MRI of the kidneys using non-rigid image registration and segmentation of voxel time courses. Comput Med Imaging Graph 2009;33(3):171–81, http://dx.doi.org/10.1016/j.compmedimag.2008.11.004.
[21] Tokuda J, Mamata H, Gill RR, Hata N, Kikinis R, Padera RF, et al. Impact of nonrigid motion correction technique on pixel-wise pharmacokinetic analysis of free-breathing pulmonary dynamic contrast-enhanced MR imaging. J Magn Reson Imaging 2011;33(4):968–73, http://dx.doi.org/10.1002/jmri.22490.
[22] Zakkaroff C, Magee1 D, Radjenovic A, Boyle1 R. Mediated spatiotemporal fusion of multiple cardiac magnetic resonance datasets for patient-specific perfusion analysis. Comput Cardiol 2010;37:469–72.
[23] Rohlfing T, Maurer CR, O'Dell WG, Zhong J. Modeling liver motion and deformation during the respiratory cycle using intensity-based nonrigid registration of gated MR images. Med Phys 2004;31(3):427–32.
[24] Song T, Lee VS, Rusinek H, Kaur M, Laine AF. Automatic 4-D registration in dynamic MR renography based on over-complete dyadic wavelet and Fourier transforms. Med Image Comput Comput Assist Interv 2005;8(Pt 2):205–13.
[25] Droske M, Rumpf M. Multiscale joint segmentation and registration of image morphology. IEEE Trans Pattern Anal Mach Intell 2007;29(12):2181–94, http://dx.doi.org/10.1109/TPAMI.2007.1120.
[26] Modersitzki J. FAIR: Flexible Algorithms for Image Registration. Philadelphia: SIAM; 2009.
[27] Pluim JP, Maintz JB, Viergever MA. Image registration by maximization of combined mutual information and gradient information. IEEE Trans Med Imaging 2000;19(8):809–14, http://dx.doi.org/10.1109/42.876307.
[28] Haber E, Modersitzki J. Intensity gradient based registration and fusion of multimodal images. In: Lecture Notes in Computer Science; vol. 4191 of Medical Image Computing and Computer-Assisted Intervention – MICCAI 2006, Lecture Notes in Computer Science. 2006. p. 726–33.
[29] Wollny G, Ledesma-Carbayo MJ, Kellman P, Santos A. Exploiting quasiperiodicity in motion correction of free-breathing myocardial perfusion mri. IEEE Trans Med Imaging 2010;29(8):1516–27, doi: 10.1109/TMI.2010.2049270.
[30] Viola P, Wells III WM. Alignment by maximization of mutual information. Int J Comput Vis 1997;24(2):137–54, doi: http://dx.doi.org/10.1023/A:1007958904918.
[31] Maes F, Collignon A, Vandermeulen D, Marchal G, Suetens P. Multimodality image registration by maximization of mutual information. IEEE Trans Med Imaging 1997;16(2):187–98, doi: 10.1109/42.563664.
[32] Pluim JPW, Maintz JBA, Viergever MA. Mutual-information-based registration of medical images: a survey. IEEE Trans Med Imaging 2003;22(8):986–1004, http://dx.doi.org/10.1109/TMI.2003.815867.
[33] Maes F, Vandermeulen D, Suetens P. Medical image registration using mutual information. Proc IEEE 2003;91(10):1699–722, doi: 10.1109/JPROC.2003.817864.
[34] Milles J, van der Geest R, Jerosch-Herold M, Reiber J, Lelieveldt B. Fully automated motion correction in first-pass myocardial perfusion MR image sequences. IEEE Trans Med Imaging 2008;27(11):1611–21, doi: 10.1109/TMI.2008.928918.
[35] Hayton P, Brady M, Tarassenko L, Moore N. Analysis of dynamic MR breast images using a model of contrast enhancement. Med Image Anal 1997;1(3):207–24, http://dx.doi.org/10.1016/S1361-8415(97)85011-6.
[36] Adluru G, DiBella EV, Schabel MC. Model-based registration for dynamic cardiac perfusion MRI. J Magn Reson Imaging 2006;24(5):1062–70, http://dx.doi.org/10.1002/jmri.20756.
[37] Melbourne A, Atkinson D, White MJ, Collins D, Leach M, Hawkes D. Registration of dynamic contrast-enhanced MRI using a progressive principal component registration (PPCR). Phys Med Biol 2007;52(17):5147, http://stacks.iop.org/0031-9155/52/i=17/a=003.
[38] Rohlfing T. Image similarity and tissue overlaps as surrogates for image registration accuracy: widely used but unreliable. IEEE Trans Med Imaging 2012;31153-163(99), http://ieeexplore.ieee.org/xpls/abs_all.jsp?arnumber=5977031&tag=1.
[39] Li X, Dawant BM, Welch EB, Chakravarthy AB, Freehardt D, Mayer I, et al. A nonrigid registration algorithm for longitudinal breast MR images and the analysis of breast tumor response. Magn Reson Imaging 2009;27(9):1258–70, http://dx.doi.org/10.1016/j.mri.2009.05.007.
[40] Buonaccorsi GA, O'Connor JPB, Caunce A, Roberts C, Cheung S, Watson Y, et al. Tracer kinetic model-driven registration for dynamic contrast-enhanced MRI time-series data. Magn Reson Med 2007;58(5):1010–9, http://dx.doi.org/10.1002/mrm.21405.
[41] Filler G, Yasin A, Medeiros M. Methods of assessing renal function. Pediatr Nephrol 2013, http://dx.doi.org/10.1007/s00467-013-2426-7.
[42] Christensen GE. Deform shape models for anatomy. Ph. D. thesis; Sever Institute of Washington; 1994.
[43] Bro-Nielsen M, Gramkow C. Fast fluid registration of medical images. Lect Notes Comput Sci 1996;1131:267–76.
[44] D'Agostino E, Maes F, Vandermeulen D, Suetens P. A viscous fluid model for multimodal non-rigid image registration using mutual information. Med Image Anal 2003;7(4):565–75.
[45] Hecke WV, Leemans A, D'Agostino E, Backer SD, Vandervliet E, Parizel PM, et al. Nonrigid coregistration of diffusion tensor images using a viscous fluid model and mutual information. IEEE Trans Med Imaging 2007;26(11):1598–612, http://dx.doi.org/10.1109/TMI.2007.906786.
[46] Kammler DW. A first course in Fourier analysis. Prentice Hall, Inc; 2000.
[47] Cahil N, Noble J, Hawkes D. Fourier methods for nonparametric image registration. In: Computer Vision and Pattern Recognition, 2007. CVPR'07. IEEE Conference on. 2007. p. 1–8.
[48] Modersitzki J. Numerical Methods for Image Registration. Oxford Science Publications;; 2004.
[49] Smith SM, Jenkinson M, Woolrich MW, Beckmann CF, Behrens TEJ, Johansen-Berg H, et al. Advances in functional and structural MR image analysis and implementation as FSL. Neuroimage 2004;23(Suppl 1):S208–19, http://dx.doi.org/10.1016/j.neuroimage.2004.07.051.
[50] Hermosillo G, Chefd'Hotel C, Faugeras O. Variational methods for multimodal image matching. Int J Comput Vis 2002;50(3):329–43.
[51] Annet L, Hermoye L, Peeters F, Jamar F, Dehoux JP, Beers BEV. Glomerular filtration rate: assessment with dynamic contrast-enhanced MRI and a cortical-compartment model in the rabbit kidney. J Magn Reson Imaging 2004;20(5):843–9, http://dx.doi.org/10.1002/jmri.20173.
[52] Sourbron SP, Michaely HJ, Reiser MF, Schoenberg SO. MRI-measurement of perfusion and glomerular filtration in the human kidney with a separable compartment model. Invest Radiol 2008;43(1):40–8, doi: 10.1097/RLI.0b013e31815597c5.
[53] Cheng HLM, Wright GA. Rapid high-resolution T1 mapping by variable flip angles: accurate and precise measurements in the presence of radiofrequency field inhomogeneity. Magn Reson Med 2006;55(3):566–74.
[54] Sourbron S. Image analysis in dce-mri. In: Proceedings of the 19th ISMRM Scientific Meeting & Exhibition In 19th ISMRM Scientific Meeting & Exhibition. 2011.
[55] Notohamiprodjo M, Pedersen M, Glaser C, Helck AD, Lodemann KP, Jespersen B, et al. Comparison of Gd-DTPA and Gd-BOPTA for studying renal perfusion and filtration. J Magn Res Imaging 2011;34(3):595–607.